AAS 25-569

REGIONS OF INFLUENCE OF EXTERIOR MEAN-MOTION RESONANCES IN THE EARTH–MOON SYSTEM: BIFURCATIONS, SEPARATRICES, AND HETEROCLINIC PATHWAYS

Anjali Rawat[*], Bhanu Kumar[†], Aaron J. Rosengren[‡], and Shane D. Ross[§]

The region beyond the Moon (within Earth's Hill sphere) hosts a complex web of exterior mean-motion resonances (MMRs) that govern the dynamics of natural and artificial bodies. We examine exterior $1{:}n$ resonances using a Poincaré map at osculating orbit apogee, expressed in orbital elements. It reveals two stable asymmetric libration zones and a weak unstable symmetric resonance zone embedded within a strong unstable symmetric region, reflecting a bifurcation due to heightened instability. The region of influence is delineated by separatrices of unstable resonant periodic orbits. Heteroclinic connections with interior MMRs via L_1-L_2 tubes are explored, enabling exterior-interior transitions and vice versa.

INTRODUCTION

The dynamics of the region exterior to the Moon are fundamentally influenced by exterior mean-motion resonances (MMRs). Quantifying the extent of the stable and unstable exterior MMRs across various semi-major axis values proceeds towards the construction of a global dynamical map. Exterior resonances at high energies (both stable and unstable) have orbits that pass between the Earth and Moon. However, purely exterior unstable resonances at lower energies have the potential to reveal low-energy pathways for transport between the interior and exterior realms[1] and have not been widely studied for the Earth–Moon system.

The exterior region is notably more chaotic than the interior,[2] exhibiting bifurcations into asymmetric resonant orbits that differ substantially from their interior counterparts. Although previous studies[2] on exterior MMRs in other celestial systems mention the existence of a separatrix, the region of influence of unstable resonant periodic orbits is not quantified. Some studies compute the widths of exterior resonances using Poincaré maps at apogee, but primarily consider low mass ratios[3] ($\mu = 10^{-3}$) and restrict attention to the libration widths of stable resonant islands, thereby neglecting the broader region of influence associated with unstable resonant orbits. In addition, most investigations focus on partially exterior resonance families,[4] which arise only at low Jacobi constants and high eccentricities, while overlooking the purely exterior low-eccentricity family and its potential to enable exterior-to-interior transfers at lower energies. Studies of Neptune's exterior resonances — with even lower mass ratios ($\sim 10^{-5}$) — have produced extensive atlases of resonance zones using Poincaré sections at perigee.[5] However, for exterior resonances at higher mass ratios, such as in the Earth–Moon system, Poincaré maps constructed at apogee experience weaker perturbations and therefore tend to offer a clearer depiction of the underlying resonant dynamics.[6] Purely exterior resonances remain unexplored at higher mass ratios, and the regions of influence associated with unstable periodic resonant orbits in both resonance zones — crucial for understanding chaotic transit through resonances — have been largely overlooked.

Building on our exploration of resonance widths, chaotic zones, and heteroclinic connections for Earth–Moon interior resonances,[7] we extend the analysis to purely exterior resonances in the Earth–Moon planar

[*]PhD Student, Aerospace and Ocean Engineering, Virginia Tech, Blacksburg, VA, United States, anjalirawat@vt.edu
[†]James Van Loo Postdoctoral Assistant Professor and NSF Postdoctoral Research Fellow, Department of Mathematics, University of Michigan, Ann Arbor, MI, United States, bhkumar@umich.edu
[‡]Assistant Professor, Mechanical and Aerospace Engineering, University of California San Diego, La Jolla, CA, United States, arosengren@ucsd.edu
[§]Professor, Aerospace and Ocean Engineering, Virginia Tech, Blacksburg, VA, United States, sdross@vt.edu

circular restricted three-body problem (PCR3BP), with the intent of facilitating a global dynamical map. Here, resonant orbits do not exist as stable-unstable pairs but as distinct asymmetric stable and symmetric unstable orbits formed as a result of bifurcation. This study computes the region of influence for prominent lunar MMRs, specifically the 1:3 and 1:4 resonances, using the PCR3BP, following the method of Koon et al.[8] By applying a Poincaré map at the apogee of osculating orbits, we delineate MMR regions in the plane of semi-major axis and synodic argument of perigee (relative to the Earth–Moon line). Our Poincaré maps reveal the 1:3 and 1:4 resonance "islands", existing as two stable asymmetric libration zones and a weak unstable symmetric libration zone, all embedded within a larger strong unstable symmetric resonance zone. After computation of the unstable resonant periodic orbits by continuation methods, the corresponding stable and unstable manifolds are visualized, forming the separatrix whose extent quantifies the region of influence of symmetric unstable resonant orbits.

We quantify regions of influence of the unstable 1:3 and 1:4 resonances across a range of Jacobi constants and project them onto the semi-major axis-eccentricity plane, overlaid with Tisserand curves. In addition, we identify a variety of weak and strong heteroclinic connections linking interior resonant orbits (2:1 and 3:1) to the 1:3 exterior resonant orbit by leveraging the tube dynamics of L_1–L_2 Lyapunov orbits, thereby demonstrating the existence of low-energy transfer pathways between interior and exterior regions. This comprehensive analysis, incorporating the full PCR3BP model, accurately delineates the true region of influence of exterior resonances of the form 1:n. These findings inform potential low-energy routes for spacecraft trajectories from the interior to exterior Earth–Moon realm — pathways that may, in turn, facilitate trajectories beyond the Earth–Moon vicinity to nearby three-body regimes, such as the Sun–Earth libration points

PLANAR, CIRCULAR, RESTRICTED THREE-BODY PROBLEM

The planar circular restricted three-body problem (PCR3BP) models a massless spacecraft moving under the gravitational influence of two primary bodies (e.g., Earth and Moon), viewed in a rotating reference frame centered at the barycenter of the two primaries. Both primaries move in circular orbits with constant angular velocity about their barycenter, and the spacecraft motion is coplanar with their orbits. In normalized units, the distance between the primaries is unity, their combined mass equals one, the period of their orbit relative to the barycentered inertial frame, i.e., the sidereal period T_m, is 2π. The system dynamics depend only on the mass ratio $\mu = \frac{m_2}{m_1+m_2}$, taken as $\mu = 1.2150584270571545 \times 10^{-2}$ for the Earth–Moon system.

We choose a coordinate frame rotating with the two massive bodies as in Fig. 1(a), centered at their barycenter with m_1 and m_2 lying on the x-axis at $(-\mu, 0)$ and $(1-\mu, 0)$, respectively. The PCR3BP differential equations of motion for the spacecraft in normalized units are then

$$\begin{aligned} \ddot{x} - 2\dot{y} &= x - (1-\mu)\frac{x+\mu}{r_1^3} - \mu\frac{x-1+\mu}{r_2^3}, \\ \ddot{y} + 2\dot{x} &= y - (1-\mu)\frac{y}{r_1^3} - \mu\frac{y}{r_2^3}, \end{aligned} \tag{1}$$

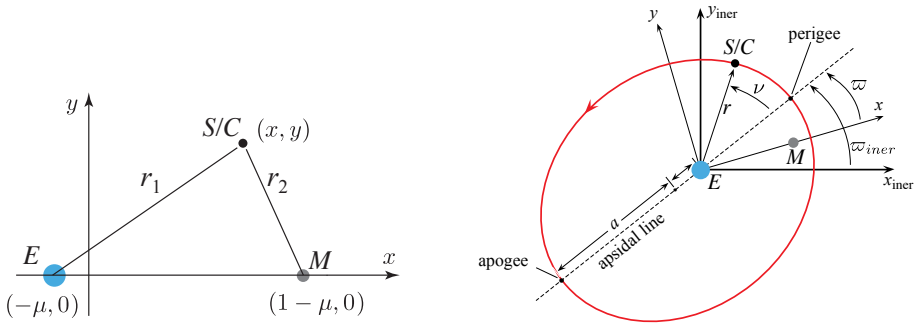

Figure 1: (a) Non-dimensional barycentered co-rotating (x, y) frame. (b) The geocentric osculating orbital elements showing inertial longitude of perigee (ϖ_{iner}) and synodic longitude of perigee (ϖ).

where $r_1 = \sqrt{(x+\mu)^2 + y^2}$ is the distance from the spacecraft to m_1 and $r_2 = \sqrt{(x-1+\mu)^2 + y^2}$ is the distance to m_2. In general, we refer to a point in the 4-dimensional, phase-space manifold $\mathcal{M}$ as X. This point can be written in terms of the rotating-frame Cartesian coordinates given above, $X = (x, y, \dot{x}, \dot{y})$. Alternatively, in the geocentric part of $\mathcal{M}$, one can use instantaneous (i.e., osculating), geocentric orbital elements, e.g., $X = (a, e, \ell, \varpi)$ where a is the semi-major axis, e the eccentricity, ℓ the mean anomaly, and ϖ the longitude of perigee with respect to the rotating frame positive x-axis, as depicted in Fig. 1(b).

Jacobi Constant and the Energy Manifold

The Jacobi constant is an integral of motion of the CR3BP equations and is proportional to the negative of the Hamiltonian energy of the system. In other words, for an initial condition $X \in \mathcal{M}$, this scalar value remains constant along the trajectory. The formula we use for the Jacobi constant of the planar problem is *

$$\mathcal{C}(x, y, \dot{x}, \dot{y}) = x^2 + y^2 + 2\left(\frac{1-\mu}{r_1} + \frac{\mu}{r_2}\right) - \left(\dot{x}^2 + \dot{y}^2\right). \tag{2}$$

Let $\mathcal{M}_C$ be the energy manifold or energy surface given by setting the Jacobi integral (2) equal to a constant:

$$\mathcal{M}_C = \{X \in \mathcal{M} \mid \mathcal{C}(X) = C = \text{constant}\}. \tag{3}$$

The surface $\mathcal{M}_C$ can be considered as a 3-dimensional manifold embedded in the 4-dimensional phase space $\mathcal{M}$. Any PCR3BP trajectory starting in $\mathcal{M}_C$ will remain therein for all time, so one can study PCR3BP dynamics restricted to each 3D manifold $\mathcal{M}_C$ separately. For the geocentric portion of $\mathcal{M}_C$ exterior to the Moon's orbit, dimensionality can be further reduced by using a 2-dimensional Poincaré surface of section at osculating orbit apogee.

Tisserand Parameter

The Tisserand approximation to the Jacobi constant in geocentric orbital elements in the CR3BP is

$$C(a, e, i) = \frac{1}{a} + 2\sqrt{a(1-e^2)}\cos i + O(\mu), \tag{4}$$

which imposes dynamical bounds on the range of motion a non-maneuvering spacecraft is capable of, depicted using the geocentric, osculating orbital elements: semi-major axis (a), eccentricity (e), and inclination (i). In the PCR3BP, the inclination is set to zero ($i = 0$). The terms of order μ, $O(\mu)$, will be ignored when the Tisserand approximation is used to plot projections of $\mathcal{M}_C$ onto (a, e) space, which appear as curves, referred to as *Tisserand curves*.

Hill Region and Hill Radius

The projection of $\mathcal{M}_C$ onto the position space (x, y) defines the Hill's region,

$$H_C = \{(x, y) \mid x^2 + y^2 + 2\left((1-\mu)/r_1 + \mu/r_2\right) \geq C\}. \tag{5}$$

with boundary ∂H_C called the zero-velocity curve, where $\dot{x} = \dot{y} = 0$. For natural (i.e., propulsion-less) trajectories, the spacecraft is restricted to remain within H_C.

There are five distinct Hill's region topologies, depending on C. In case 2 ($C_1 > C > C_2$), a bottleneck opens at L_1, allowing Earth–Moon transitions. In case 3 ($C_2 > C > C_3$), see Fig. 2(a), an additional bottleneck opens at L_2, permitting transitions from Earth realm to the exterior realm using L_1-L_2 Lyapunov orbit tubes. This will be explored in the heteroclinic connections section. The region which lies outside the shaded forbidden region is the *exterior realm* surrounding the Earth (and Moon), largely dominated by exterior MMR geocentric orbits (with Earth the dominant mass), up to the Earth's sphere of influence.

*We note that this definition differs from some authors, who add a constant value $\mu(1-\mu)$, so that the Jacobi constant of the L_4, L_5 points is precisely 3. We adopt the convention in current use among the cislunar astrodynamics community.

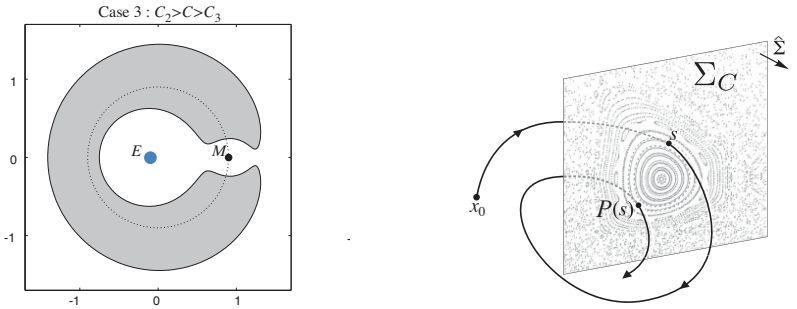

(a) (b)

Figure 2: (a) Case 3 of the Hill's regions H_C in the Earth–Moon rotating (synodic) frame. (b) Poincaré map P on a Poincaré section Σ_C in the CR3BP. The unit vector $\hat{\Sigma}$ gives the sense in which trajectories are crossing Σ_C.

Earth's sphere of influence or Hill radius is given by,

$$R_H \approx a_e \sqrt[3]{\frac{m_e}{3(m_e + m_s)}} \approx 3.9034\, NDU \tag{6}$$

where, a_e is the semi-major axis of the Earth with respect to the Sun, m_e is the mass of the Earth and m_s is the mass of the Sun. We will see in our results that the exterior MMRs, largely lie within Earth's Hill radius with 1:4 marking the boundary.

THE POINCARÉ MAP AND KEY DYNAMICAL FEATURES

Surface of Section at Apogee

To study exterior MMRs, we use the Poincaré surface of section at apogee with crossings identified when the geocentric mean anomaly ℓ (and true anomaly ν) are π. We choose an apogee surface of section as apogee faces less perturbations in the exterior realm and produces a better picture of resonant dynamics.[6] Our Poincaré section, parametrized by Jacobi constant C, is defined as,

$$\Sigma_C = \{X \in \mathcal{M}_C \mid \ell = \pi\}. \tag{7}$$

In practice, to avoid numerical problems in detecting section crossings during propagation, we consider a continuous function of the mean anomaly that is zero at $\ell = \pi$. The Poincaré section so constructed is 2D, and can be represented by two coordinates that can be interpreted in orbital-element space: the semi-major axis a and the synodic longitude of perigee ϖ, the angle between perigee and the Moon's location in the rotating frame (see Fig. 1). As ϖ is an angular variable, Σ_C has a cylindrical topology, i.e., $(\varpi, a) \in S^1 \times I$ where $I \subset \mathbb{R}$, and S^1 is the circle.

Poincaré Map on the Poincaré Section

Poincaré maps simplify the study of the PCR3BP by transforming a 4-dimensional phase space into a more manageable 2-dimensional analysis, elucidating periodic, quasi-periodic, and chaotic behaviors, and revealing the intricate manifold structures that govern the system's dynamics.

The section Σ_C represents a 2-dimensional surface transverse to the flow inside the energy manifold $\mathcal{M}_C$ (cf. Fig. 2(b)). Let $x_0 \in \mathcal{M}_C$ denote an initial state, not necessarily in Σ_C. The Poincaré map $P(x_0) = s$ corresponds to the first crossing of Σ_C by the trajectory originating at x_0 in a particular direction. In general, we will consider Poincaré mappings of Σ_C to itself,

$$\begin{aligned} P : \Sigma_C &\to \Sigma_C, \\ s &\mapsto P(s). \end{aligned} \tag{8}$$

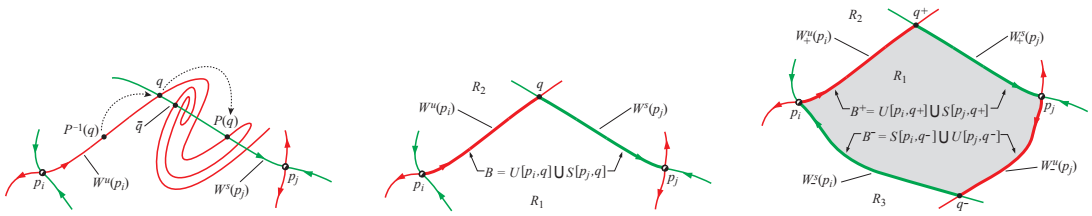

Figure 3: (a) PIP (q) and secondary intersection point ($\bar{q}$, not a PIP). (b) A BIP q defining a local boundary B between two regions R_1 and R_2. (c) Top and bottom boundary to a resonance region R_1.

As described in Rawat et al,[7] the "orbit" of a point $s \in \Sigma_C$ under P is the set of all the past and future iterates of the point s under the map P. The orbits that have a finite sequence of points $\mathcal{O}(p_n) = p_1, \ldots, p_n$, are periodic orbits of P, i.e., sequence repeats after some definite iterate. This represents a continuous periodic PCR3BP trajectory, a closed loop, within $\mathcal{M}_C$. These periodic orbits are referred to as fixed points on the map, as the state returns to the initial point $p_1 \in \Sigma$ after n iterates P^n of the Poincaré map.

If a periodic orbit is of center-type, that denotes a stable resonant orbit. Its stable fixed point will have quasi-periodic orbits of P^n surrounding it on the Poincaré Map. The extent of the largest invariant tori, in semi-major axis gives the stable resonance width of that particular resonance. If a periodic orbit is of saddle-type, it denotes an unstable resonant orbit. It will have attached stable $(W^s(p_i))$ and unstable $(W^u(p_i))$ invariant manifolds, for $i = 1, \ldots, n$, consisting of orbits of P which tend asymptotically toward $\mathcal{O}(p_n)$ forwards or backwards in time, respectively. It is known that for 2D Poincaré maps of 2 degree-of-freedom Hamiltonian systems,[9,10] some periodic orbits $\mathcal{O}(p_n)$ are related to a general idea of "resonance", even beyond just orbital dynamics applications.

A resonance zone — the region of influence of an unstable MMR — can be defined via the stable and unstable manifolds of $\mathcal{O}(p_n)$ which are 1-dimensional curves within the 2D Poincaré section Σ_C. An intersection point of the stable and unstable manifolds of the saddle-type periodic orbit $\mathcal{O}(p_n) = \{p_1, \ldots, p_n\}$ is termed a primary intersection point (PIP), denoted by q in Fig. 3(a). All past and future iterates of a PIP are also PIPs.[11] Intersections between stable and unstable invariant manifolds of the same periodic orbit mark homoclinic points as they enable homoclinic transfers.

We use PIPs to define *boundaries*, sometimes called separatrices, and subsequently resonance regions. As a matter of convention, for a boundary intersection point, BIP, we pick the PIP with the shortest arc-length of the manifolds, measured from the fixed points to the intersection point, dividing the Poincaré section Σ_C into distinct regions R_1 and R_2, as illustrated in Fig. 3(b). As there are always two branches each for a stable and unstable manifold, we can identify both a "top" and "bottom" boundary by choosing BIPs, q^+ and q^- respectively. These boundaries enclose a closed *resonance region*, R_1, as shown in Fig. 3(c).

Within our cylindrical Poincaré section Σ_C, we can have multiple resonance regions. For our purposes, we will quantify the resonance zones by measuring the maximum/minimum extent in semi-major axis of the stable and unstable manifold when followed forward and backwards respectively, from the BIP to the unstable fixed points, both at the top/bottom boundary.

Unless constrained by other barriers within Σ_C such as rotational invariant curves (RICs)[12–14] — quasi-periodic KAM tori that block transport along semi-major axis in the cylindrical phase space of Σ_C — there can be intersections between stable and unstable manifolds of different periodic orbits. Such intersections are denoted as *heteroclinic* points and enable heteroclinic transfers.

UNSTABLE PERIODIC ORBITS AND MANIFOLDS

To understand the structure of unstable resonant orbit families and the heteroclinic dynamics induced by them, one needs to compute the corresponding periodic orbits as well as their stable/unstable manifolds. A mean-motion resonance denoted as $k{:}k_m$ is characterized by the ratio of orbital periods where k and k_m

denote coprime positive integers representing the number of spacecraft and Moon geocentric orbits completed with respect to an Earth-centered inertial frame. In this paper, we study exterior resonances, where $k < k_m$. To compute a family of k:k_m unstable periodic orbits in the Earth–Moon PCR3BP, we start with an orbit state from the Earth Kepler problem having semi-major axis a such that $(a/a_m)^{3/2} = (k_m/k)$, where $a_m = 1$ in non-dimensional units. For strong unstable resonant periodic orbits, the initial longitude of periapsis $\bar{\omega}$ and true anomaly ν are both taken as 0; for weak unstable orbits, the initial values are $\bar{\omega} = \pi$ and $\nu = 0$ (strong and weak instability will be discussed later). This orbit will be symmetric about the x-axis and will also be periodic in the rotating Kepler problem (i.e., PCR3BP with $\mu = 0$). Thus, the method of perpendicular x-axis crossings can be used to numerically continue this Keplerian orbit to the true value of $\mu = 1.215058427057154 5 \times 10^{-2}$ for the Earth–Moon system; see, for example, Section 2.6.6.2 of Parker and Anderson[15] for details of this method. The same method is then used to continue the resulting PCR3BP orbit through the rest of its orbit family, using the perpendicular orbit x-intercept as the continuation parameter.

Once the periodic orbits in a family k:k_m have been computed, the computation of their stable/unstable manifolds is carried out using techniques developed by the second author.[?,16–18] In particular, we compute the intersection of these manifolds with the previously mentioned apogee Poincaré surface of section Σ_C. Such sections, utilizing osculating orbital elements, have been used by, e.g., Ross and Scheeres[13] and Howell et al.[19] as well; they have better transversality to the PCR3BP flow as compared to other commonly used sections such as $y = 0$. When using such a section in the exterior realm, the periodic orbit intersection points with the section are period-k fixed points of the Poincaré map P. This is because such an k:k_m orbit passes through apogee k times during one period, which takes approximately k_m lunar sidereal periods. This implies that all resonant orbits of the form 1:n are period-1 fixed points of the Poincaré map P. The portions of the periodic orbit stable/unstable manifolds lying in the chosen Poincaré section will correspond to 1D curves. Intersections of the 1D manifold curves will provide the geometry (e.g., PIPs, BIPs, homoclinic points, heteroclinic points) as discussed previously.

EXTERIOR RESONANCE AND KEY DYNAMICAL FEATURES

An exterior mean-motion resonance is denoted by the ratio k:k_m, where $k < k_m$ and each denote co-prime positive integers representing the number of spacecraft and Moon geocentric orbits completed with respect to an Earth-centered inertial frame, respectively. Expressed in terms of the inertial-frame period of the spacecraft, T, and the sidereal period of the Moon, T_m, we have an approximate relationship, $T/T_m \approx k_m/k$, within the context of the CR3BP.

In terms of the Poincaré map and section pair described above, (P, Σ_C), a resonant orbit is a period-k orbit which takes approximately k_m sidereal lunar periods. For exterior resonances of the form 1:n, the resonant orbit will always be a period-1 fixed point on the map.

Poincaré Map Computation at Apogee

To compute the Poincaré map at the osculating orbit's apogee for a given Jacobi constant, initial conditions are selected along the negative x-axis ($x < -1$, $y = 0$), positioned beyond the radius of the Moon. A sufficiently broad range of $\dot{x}$ values is chosen, from which corresponding values of $\dot{y}$ are derived using Eq. 2. Crossings are specifically recorded at the apogee because, in the exterior region, the spacecraft is minimally perturbed by lunar influences at apogee, offering more robust identification of Poincaré section crossings and clearer insight into resonant dynamics.[6]

The resulting Poincaré map, exemplified in Fig. 4 at a Jacobi constant $C = 3.25$, shows multiple stable islands, distinctly two separate asymmetric 1:3 and small 1:4 resonance islands, surrounded by an extensive chaotic sea within which are embedded unstable resonant orbits. The underlying structure of the chaotic sea for unstable resonant orbits is revealed by following the methodology of unstable orbit determination and manifold computation mentioned in the previous section. We identify a weak unstable resonant orbit with its "quasi-separatrices"[20] surrounding the two stable asymmetric islands embedded within the separatrices of a larger strong unstable resonant orbit. The features of the identified structures will be discussed ahead. Furthermore, no trajectories are observed below a certain critical semi-major axis, clearly demarcating the boundary imposed by the energy surface.

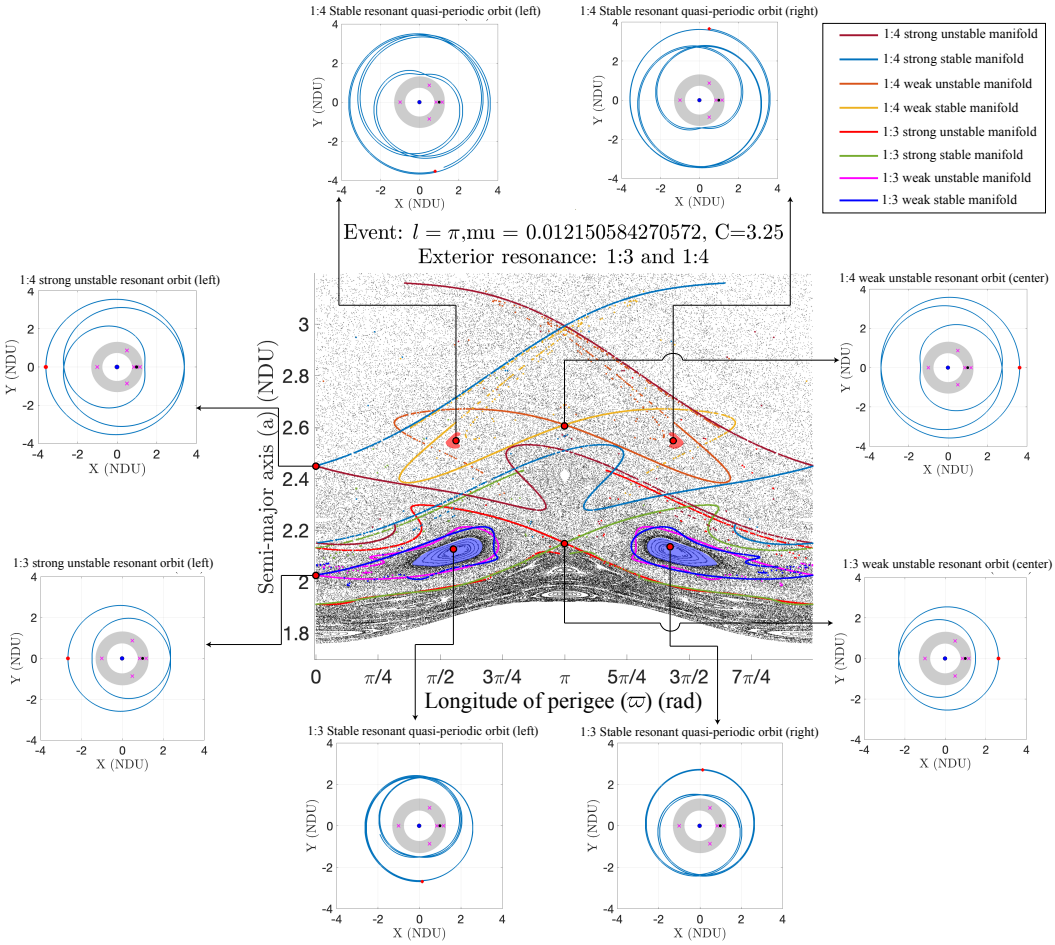

Figure 4: Poincaré Map for C=3.25 showcasing 1:3 and 1:4 exterior resonances with stable and unstable manifolds emerging from two symmetric strong and weak unstable resonant orbits surrounding two asymmetric stable resonant orbits.

Additionally, Poincaré maps computed using the surface section defined by $y = 0$ and $\dot{y} < 0$ further illuminate resonance structure by revealing the order of resonance. For instance, see Fig. 5, while the apogee section for the stable asymmetric 1:3 resonance demonstrates a single island, the $y = 0$ section presents two islands for $\varpi < \pi$, matching the resonance order, 2. Similarly, the $y = 0$ section for the stable asymmetric resonance of 1:4 manifests three islands, again corresponding to its resonance order, despite the apogee section still displaying only a single island in 4. The number of isolated islands in the apogee map indicates the numerator (k) of the resonance, whereas the island count on the $y = 0$ surface reveals the resonance order $|k_m - k|$. Utilizing this methodology we can identify the stable resonances on the given map to be 2:5, 3:8, 1:3, 2:7 and 1:4 exterior resonances. This can be further verified by computing the theoretical relation $a = (k_m/k)^{2/3}$ which should be close to the semi-major axis of the resonance center.

Asymmetric stable orbits – $1 : n$ **type**

Poincaré sections typically reveal two major categories of stable islands: symmetric and asymmetric. Symmetric resonances have at least one resonant center located at either $\varpi = \pi$ or $\varpi = 0$, exemplified by resonances such as 2:5, 3:8, and 2:7, arranged in ascending semi-major axis order. Conversely, asymmetric resonances possess resonant centers located at values of ϖ distinct from 0 or π. It is well-established that resonances of type $1 : n$ in the exterior region are inherently asymmetric,[2] forming pairs of disconnected stable islands without symmetry around either axis. Fig. 4 highlights dominant asymmetric islands, notably those associated with the 1:3 resonance, accompanied by smaller emerging islands related to the 1:4 reso-

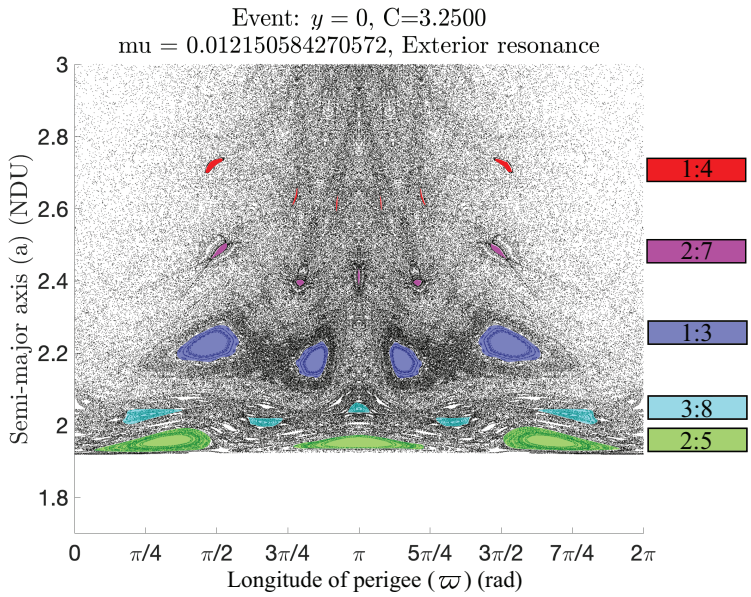

Figure 5: Poincaré Map at $y = 0$ for C=3.25 showcasing 2:5, 3:8, 1:3, 2:7 and 1:4 exterior resonances showcasing the order of resonance

nance, along with trajectories of their quasi-periodic orbits in rotating frame. These asymmetric orbits emerge through bifurcations involving stable and weakly unstable orbits, as elaborated in the next section.

Standard differential correction techniques relying on orbital symmetry[8,15] are inadequate for computing asymmetric stable resonant periodic orbits. The second author thus very recently developed a suitable methodology[21] to calculate such asymmetric orbits; its use for computation of asymmetric resonant orbits is work in progress.

Strong and weak unstable resonant periodic orbits

As previously discussed, a strong unstable resonant periodic orbit can be computed by starting with a semi-major axis defined by the required resonance ratio and a configuration where initial longitude of periapsis and true anomaly are both 0, and continuing it along μ for the Earth–Moon system. Similarly, weak unstable resonant orbits can be computed by starting with a configuration with initial longitude of the periapsis at π and true anomaly at 0. Starting with a near-circular orbit in each MMR weak unstable periodic orbit family, we find that the very low-eccentricity orbits in such families are actually stable and belong to the apocentric libration zone;[3] however, upon decreasing the perigee on the side 180 degrees opposite from the Moon (thus increasing eccentricity), the stable orbit family very quickly undergoes a bifurcation where the non-trivial planar stable eigenvalue pair passes through 1 and becomes mildly unstable. The resulting orbits are the symmetric weak unstable resonant orbits. As the Jacobi constant does not reach an extremum at this bifurcation, it must also generate[22] an additional pair of asymmetric periodic orbit families, which are the asymmetric stable resonant orbits described earlier.

The separatrices of 1:n unstable exterior resonances exhibit a notable contrast to interior resonances, with more complex and richer chaotic dynamics. Two asymmetric stable islands are enclosed between the quasi-separatrices of a symmetric weak unstable resonant orbit. This entire structure is embedded within the separatrices of a symmetric strong unstable orbit, which also defines the region of influence of unstable mean motion resonance. The quasi-separatrices of the weak unstable orbits are not the separatrices of the whole resonance region. They are contained inside the libration zone, at least for lower eccentricities, but eventually they start intersecting the separatrices of the strong unstable orbits and get scattered.

The structure of separatrices varies markedly with the Jacobi constant. For instance, in the 1:3 resonance at the chosen Jacobi constant (Fig. 4), the weak unstable orbit's quasi-separatrices are single-lobed and

remain distinct from the strong unstable orbit's separatrices even after prolonged iterations, indicating limited chaotic transport. Conversely, the 1:4 weak unstable resonant orbit exhibits multi-lobed quasi-separatrices with turnstiles intersecting the strong unstable separatrices at multiple points, revealing complex heteroclinic interactions *within a single MMR*. As detailed in subsequent results, such separatrix structures significantly evolve with changing Jacobi constants, with lower Jacobi constants (higher energies) exhibiting enhanced interaction and chaotic mixing between weakly and strongly unstable manifolds compared to higher Jacobi constants (lower energies).

DIRECT IDENTIFICATION OF RESONANCE ZONES

The Poincaré map at apogee reveals stable resonant orbits as fixed points surrounded by stable quasi-periodic librational tori. These stable islands appear in the midst of a chaotic sea which is not featureless but has embedded unstable resonant orbits and their corresponding separatrices that govern chaotic dynamics and can quantify the region of influence of a particular MMR. The dynamics of motion into and out of the resonance region are determined by lobe dynamics not addressed here,[8] but documented elsewhere.[23–27]

As described in Rawat et al,[7] the resonance widths are given by the extent of outermost invariant tori of stable islands in the (ϖ, a) plane. The influence of the resonance region extends beyond the outermost stable resonance librational torus regions to the "separatrix", the boundary formed by the intersection of stable and unstable manifolds. Particularly in the case of exterior resonance we see a rich and complex structure of the quasi-separatrices of weak unstable resonant orbits embedded within separatrices of strong unstable resonant orbits which are characterized by complex lobe structures that change form with Jacobi constants.

The region of influence of the resonance—the resonance zone—is defined by spread in semi-major axis of the separatrices of the strong unstable resonant orbit. The BIP of the separatrices is identified. Following the stable and unstable manifold forward and backward respectively, from the BIP to the strong unstable fixed point and noting down the maximum extent of the top boundary and the minimum extent of the bottom boundary in semi-major axis gives us the resonance zone. This is depicted in Fig. 6; an improvement of the

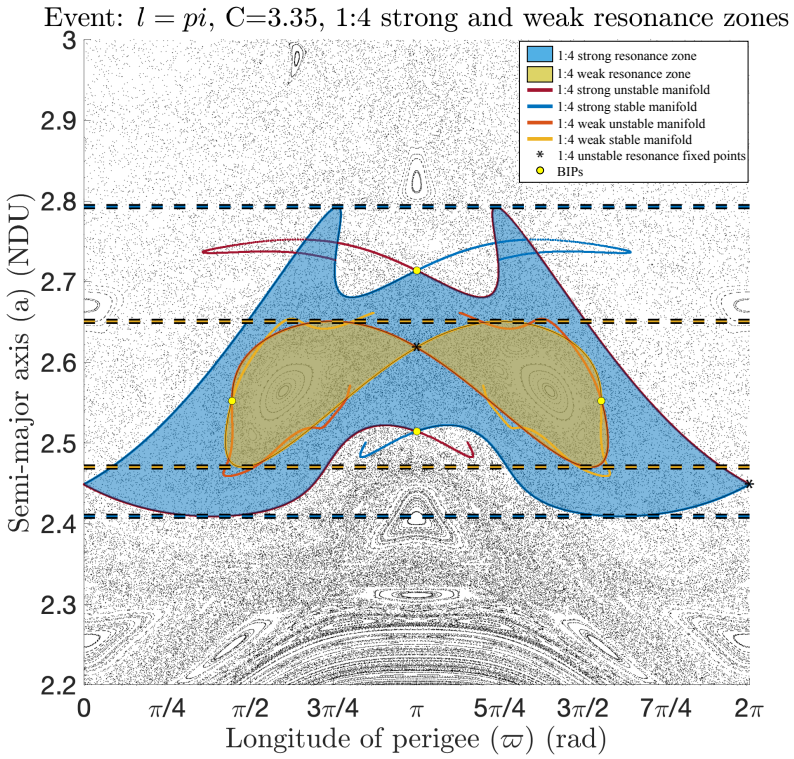

Figure 6: Schematic for identification of resonance zones using a Poincaré map at apogee for $C = 3.35$ showcasing 1:4 strong and weak resonance zones.

definition in Rawat et al,[7] as the extent of the boundary defined by the BIP would correctly denote the region of influence of unstable resonant orbits, as it also incorporates lobes. The region of influence of the weak unstable resonant orbits can also be defined using its quasi-separatrices in the same manner but are not the separatrices of the whole resonance region as they are contained inside the libration zone, at least for lower eccentricities. Eventually they start intersecting the outer separatrices and get scattered chaotically as seen in Fig. 7.

Poincaré maps are systematically computed over a range of Jacobi constants, specifically spanning from $C = 1.5$ to $C = 3.57$. Select illustrative maps for the interval $C = 3.15$ to $C = 3.35$ are presented in Fig. 7. For lower values of the Jacobi constant, specifically below $C = 3.20$, the asymmetric stable islands associated with the 1:3 resonance remain notably small. At these higher energies, the quasi-separatrices of the 1:3 weakly unstable orbit extensively intersect with the outer separatrices of the strongly unstable 1:3 resonant orbit, covering substantial regions within phase space. An analogous scenario is observed for the 1:4 resonance, where stable islands remain small up to around $C = 3.25$. Below this critical value, intersections between quasi-separatrices and separatrices of weak and strong unstable resonant orbits, respectively, again become pronounced, significantly expanding the weak unstable resonance region's domain of influence.

Analyzing these Poincaré maps becomes increasingly complex due to the chaotic interplay of intersecting manifolds. Nevertheless, certain characteristic structures remain discernible. Specifically for $C = 3.25$, see Fig. 7, separatricies of 1:3 strong resonant orbit are plotted for more iterations to show that it features self-intersecting, multi-lobed turnstiles. Such intricate turnstile structures complicate calculations of transport phenomena and the quantification of lobe areas, critical for understanding mass exchange between different dynamical regions.

Fig.7 illustrates, as an example, how the position of the BIPs associated with the strongly unstable 1:4 resonant orbit varies in terms of the semi-major axis with changes in the Jacobi constant. This variation has direct implications for the resonance zone widths, as will be discussed in subsequent sections.

Furthermore, a notable structural evolution is observed in the 1:2 stable resonance island between $C = 3.10$ and $C = 3.15$, where a 1/4-type bifurcation occurs. This bifurcation significantly modifies the stable islands' configuration within phase space, aligning closely with the predictions described by Greene's criterion concerning the breakup of invariant tori.[28]

Both 1:3 and 1:4 weak unstable periodic orbits belong to single continuous families – 1:3 weak unstable family ranges from $C = -0.56$ up to $C = 3.37$, 1:4 weak unstable family ranges from $C = -0.35$ up to $C = 3.57$. However, the strong unstable periodic orbits for both MMRs are contained across three separate families – low eccentricity (Family 1), mid eccentricity (Family 2) and high eccentricity (Family 3) family.

The low eccentricity family that stay purely in the exterior realm and exist only for higher Jacobi constant values or lower energies – $C = 3.13$ to $C = 3.57$ for 1:4 strong unstable resonance and $C = 3.09$ to $C = 3.36$ for 1:3 strong unstable resonance. The high eccentricity family whose orbit enters the region between the Earth and Moon and exist for lower Jacobi constant values or higher energies – $C = 1.50$ to $C = 2.81$ for 1:4 strong unstable resonance and $C = 1.50$ to $C = 2.84$ for 1:3 strong unstable resonance. There is yet another resonance zone that describe mid-eccentricity family where the orbit enters the Moon realm but not the interior region. This exists for mid Jacobi constants values and has highly unstable orbits with monodromy matrix eigenvalues on the order of several thousands – $C = 2.82$ to $C = 3.11$ for 1:4 strong unstable resonant orbits and $C = 2.86$ to $C = 3.08$ for 1:3 strong unstable resonant orbits.

While the resonances are identified and depicted in (ϖ, a) space, we would also like to depict them in the (a, e) plane, as this helps us visualize the resonance widths and resonance zones globally for different Jacobi constants. The Poincaré section points, which are actually 3-dimensional points (a, e, ϖ) for each C, can be projected into the (a, e) plane as in Fig. 8. Tisserand curves are an approximation to the projection of an energy surface $\mathcal{M}_C$ onto the (a, e) plane. This approximation does not perform well in the exterior regime.

A key characteristic unique to exterior resonances, observed clearly in the (ϖ, a) plane, is the distinct curvature of the resonance islands. Unlike interior resonance islands, which typically align straight along semi-major axis, these exterior islands exhibit a downward tilt from either sides. When represented in the (a, e) plane, these data points deviate noticeably from the theoretical Tisserand approximation curve, exhibit-

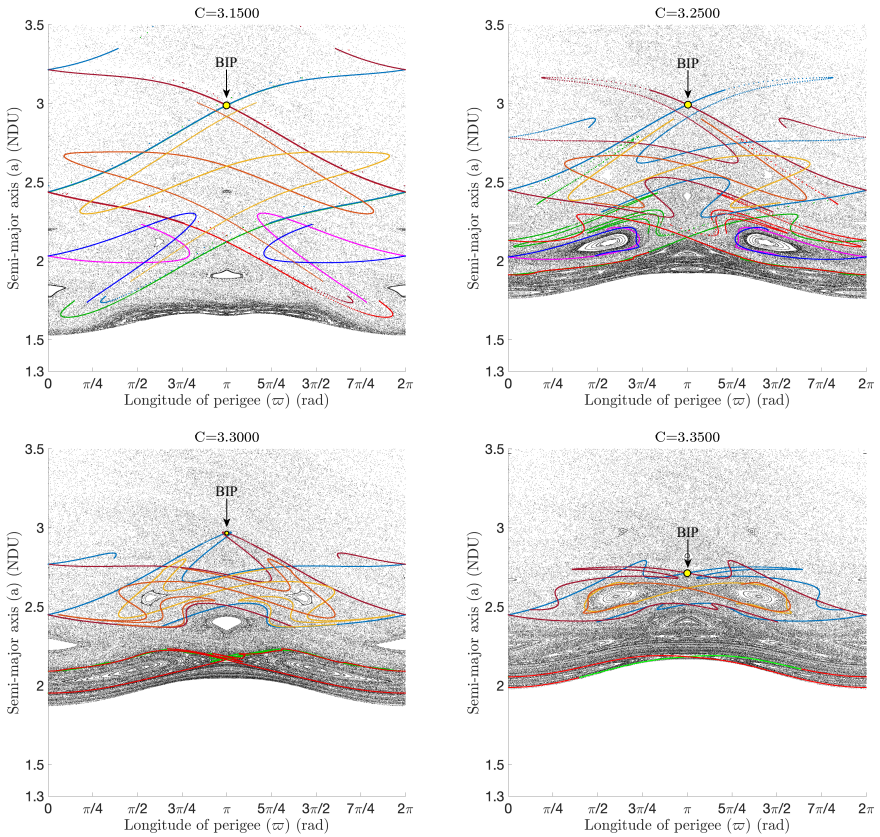

Figure 7: Poincaré sections Σ_C along with manifolds of 1:3 and 1:4 weak and strong unstable resonant orbits for 3.15, 3.25, 3.30, and 3.35. Variations in the structure of separatrices and variation in the location of BIP for 1:4 strong resonant orbit is shown as Jacobi constant increases.

ing finite width in eccentricity. This indicates that trajectories sharing an identical semi-major axis possess a continuum of eccentricities governed by the longitude of perigee, reaching minimum eccentricity at $\varpi = \pi$ and increasing as ϖ moves toward 0 or 2π. Fig. 8 showcases this observed phenomenon by viewing the Poincaré map in (a, e, ϖ) space and projecting it into three distinct planes.

The Poincaré section points are projected onto the (a, e) plane, marking weak and strong resonance zones for the 1:3 and 1:4 resonances. Figs. 9, 10, 11 and 12 show the resonance zones for 1:3 strong, 1:3 weak, 1:4

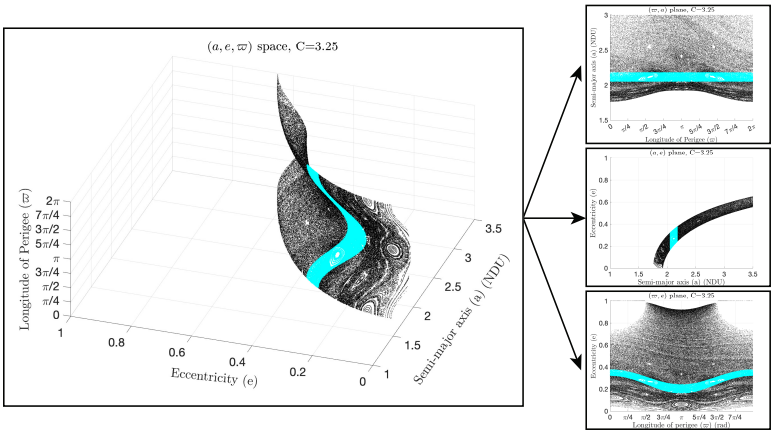

Figure 8: Poincaré Map at $l = \pi$ for C=3.25 viewed in (a, e, ϖ) space and projected onto (ϖ, a),(a, e) and (ϖ, e) planes. Cyan color represents bands of constant values of semi-major axis.

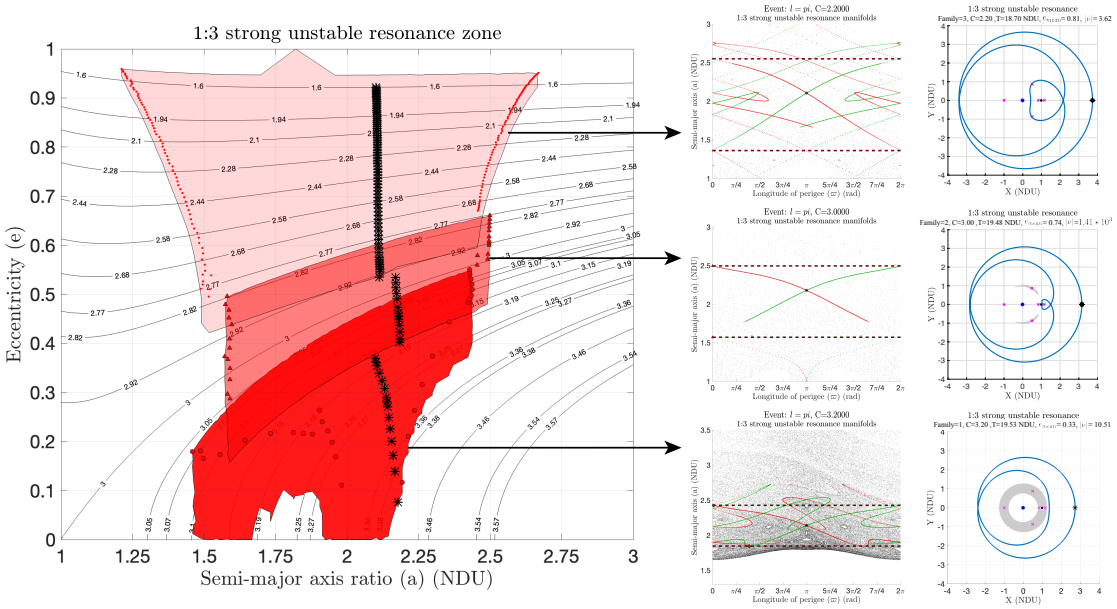

Figure 9: Resonance zones for 1:3 strong unstable resonant orbits for $C = 1.50$ to $C = 3.34$ in increments of 0.02, shown in the (a, e) plane. Three different families are observed. Manifolds and unstable orbits in rotating frame are plotted for mean Jacobi constant for each family.

strong and 1:4 weak unstable resonances, respectively. For strong unstable resonance zones, three different families are depicted, marked distinctly by different semi-major axis of unstable resonant orbits. For weak unstable resonance a single continuous family is shown. Poincaré maps for near mean Jacobi constant of a family along with separatrices of unstable resonant orbit and the trajectory of the unstable resonant orbit is depicted as insets. Since the Poincaré map projected on (a, e) plane has a certain width as illustrated in Fig.

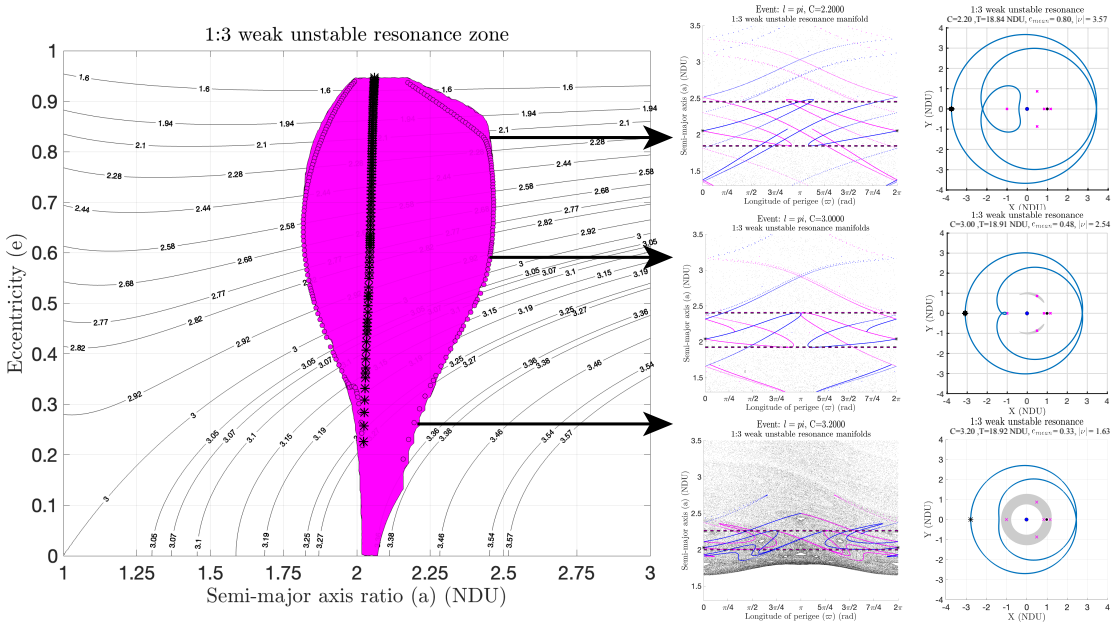

Figure 10: Resonance zones for 1:3 weak unstable resonant orbits for $C = 1.50$ to $C = 3.34$ in increments of 0.02, shown in the (a, e) plane. This belongs to a single family. Manifolds and unstable orbits in rotating frame are plotted for mean Jacobi constants of Fig. 9.

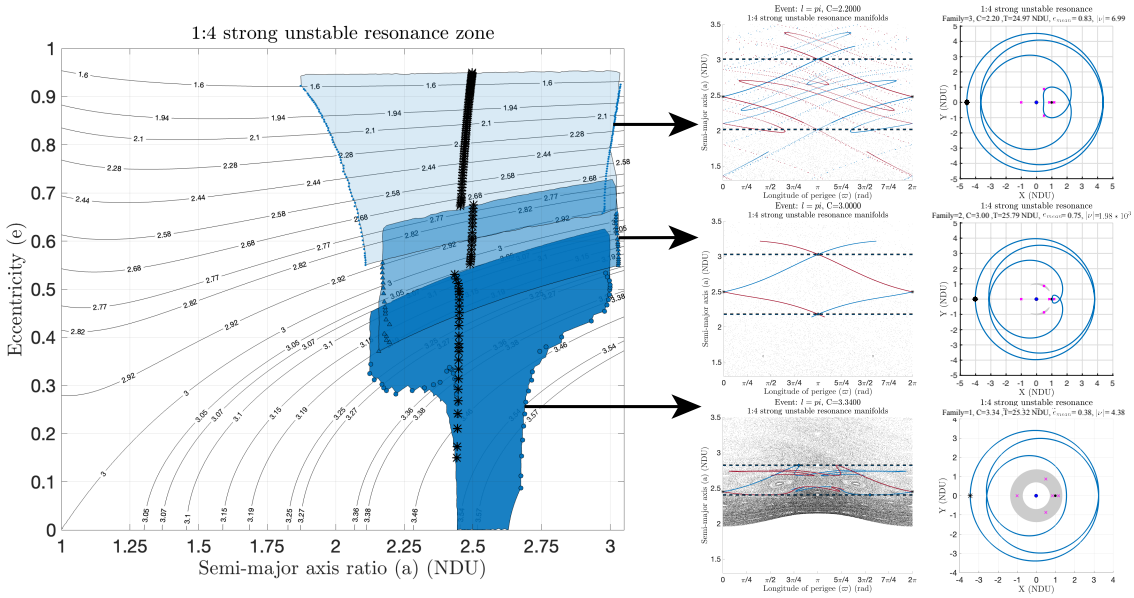

Figure 11: Resonance zones for 1:4 strong unstable resonant orbits for $C = 1.50$ to $C = 3.50$ in increments of 0.02, shown in the (a, e) plane. Three different families are observed. Manifolds and unstable orbits in rotating frame are plotted for mean Jacobi constant for each family.

4, the exact position of the BIPs in the (a, e) plane lies enclosed within the resonance zone boundary.

The time period, stability parameter and the mean eccentricity for the unstable orbit shown in the insets is computed. The stability parameter is given by the expression, $\nu = \frac{1}{2}(\lambda + 1/\lambda)$, where λ is the eigenvalue corresponding to stable or unstable manifold. For strong unstable resonant orbits of both 1:3 and 1:4 unstable resonance, the mid-eccentricity family is the most unstable, with stability parameters varying in the range of thousands. For the low-eccentricity and high-eccentricity family the stability parameter increases as they approach the Jacobi constant range of the mid-eccentricity family. For weak unstable resonant orbits of both 1:3 and 1:4 unstable resonance, the range of stability parameter values is very less and varies proportionally to the width of the resonance zone, with more unstable towards the middle and less unstable at the top and bottom values of the Jacobi constant. The time period varies minimally across all resonance zones of a particular resonance.

The resonance zones are broader for lower Jacobi constants and taper towards the bottom as Jacobi constant increases for both strong and weak unstable resonances. For the low-eccentricity family in both 1:3 and 1:4 strong resonance zones we observe a funnel type shape. This is because the position of the BIP changes as we move across those Jacobi constant values as seen in Fig. 7. At higher Jacobi constants the lobes formed by the separatrices are small and do not intersect, while at lower Jacobi constant values, the lobes are very large and intersect at BIPs corresponding to a wider semi-major axis range.

The resonance zones of 1:3 and 1:4 resonance occupy a very large area of exterior regime. Taken together, the 1:3 and 1:4 resonance regions span approximately 735,511 km ($\approx$ 2 NDU) in semi-major axis, depicting how they predominantly occupy the exterior realm.

All the 1:3 and 1:4 resonance zones are overlapped onto a single (a, e) plane, as shown in Fig. 13. There is considerable overlap between the weak and strong unstable resonance zones which is also evident from the (ϖ, a) plane, see Fig. 7. This overlap gives rise to multiple heteroclinic connection between the weak and strong unstable resonant orbit of the same as well as different MMRs. The weak unstable resonance zone is always enclosed within the strong unstable resonance zone, indicating that the region of influence of the strong unstable resonance is always more dominant.

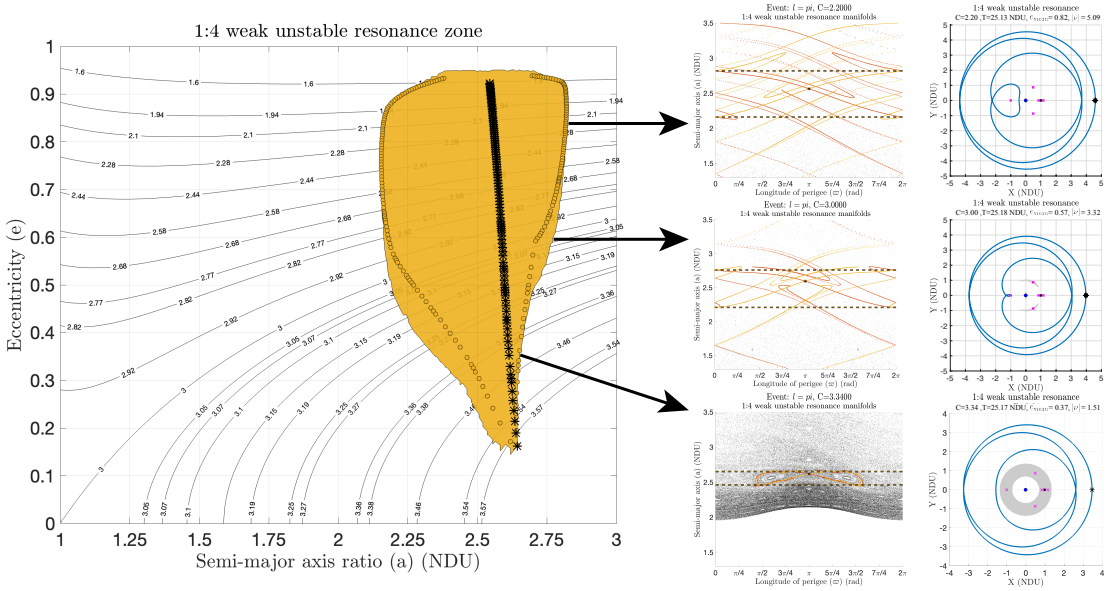

Figure 12: Resonance zones for 1:4 weak unstable resonant orbits for $C = 1.50$ to $C = 3.50$ in increments of 0.02, shown in the (a, e) plane. This belongs to a single family. Manifolds and unstable orbits in rotating frame are plotted for mean Jacobi constants of Fig. 11.

Progress in discerning the influence of specific predominant resonances, such as the 1:3 and 1:4 MMRs in the exterior regime, through the PCR3BP, contributes to advancing our understanding of these lunar resonances and in the formation of a global cislunar dynamical map.

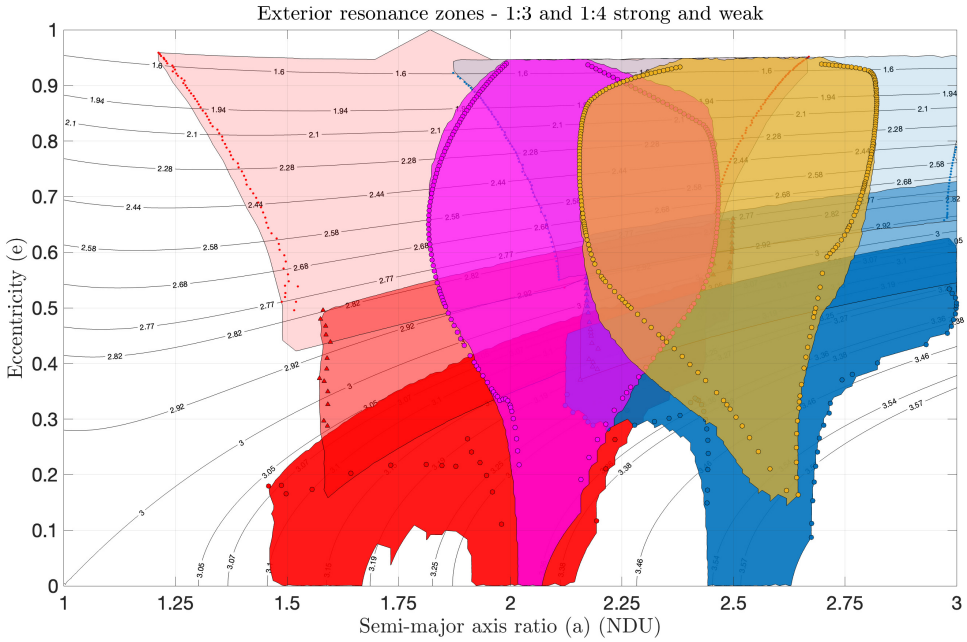

Figure 13: Resonance Zones for 1:3 and 1:4 strong and weak, $C = 1.50$ to $C = 3.56$ in increments of 0.02, shown combined in the (a, e) plane.

HETEROCLINIC CONNECTION BETWEEN EXTERIOR AND INTERIOR RESONANCE USING L_1 AND L_2 TUBES

As described in the previous section, several heteroclinic connections exist between 1:3 and 1:4 unstable resonant orbits because of considerable overlap of their resonance zones that enable inter-resonance transfers. However, more intriguing and of practical use to satellite dynamics are transfers between interior and exterior realms, at energies sufficiently low for the L_1 and L_2 bottlenecks to open.

As first noticed in Koon et al. 2000[29] and elaborated upon in 2001[1] and 2003,[30] intersections between "lobes" related to invariant manifold of unstable MMR periodic orbits and "tubes" associated with L_1 Lyapunov orbits can be used to design low-energy trajectories between Earth orbits and lunar orbits (also recently used by Hiraiwa et al. 2024[31] and Rawat et al. 2024[7]). Similar analogies can be drawn for intersections between "lobes" related to invariant manifolds of exterior unstable MMR periodic orbits and "tubes" associated with L_2 Lyapunov orbits to design low-energy trajectories between exterior orbits, lunar orbits and even interior orbits.

The L_2 Lyapunov orbit stable and unstable manifolds each have two branches: one extending toward the Moon realm and one toward the exterior realm. Similarly, both manifolds of the L_1 Lyapunov orbit have two branches: one extending toward the Earth realm and one toward the Moon realm. These manifolds serve as *co-dimension-one separatrices* within the constant energy surface $\mathcal{M}_C$, partitioning transit and non-transit trajectories. Trajectories inside these tubes execute transit orbits, (Earth-to-Moon)/(Exterior-to-Moon) or their time-reversed counterparts (Moon-to-Earth)/(Moon-to-Exterior). 14(a)) showcases only those branches of tubes that enable transfer from exterior to interior. The apogee cut of the stable manifold tube in the exterior and the perigee cut of the unstable manifold tube in the interior are depicted (black curves) to help visualize further results Trajectories that originate externally enter the lunar domain via the stable manifold tube of the L_2 Lyapunov orbit and subsequently exit through its corresponding unstable manifold tube. Within the lunar region, a sophisticated interplay emerges, characterized by the intermingling of the unstable manifold tube of the L_2 Lyapunov orbit and the stable manifold tube of the L_1 Lyapunov orbit, as illustrated in Fig. 14(b).

To systematically analyze this manifold intermingling, we construct a Poincaré section at the plane $x = 1 - \mu$, tracking the first crossing of the unstable manifold of L_2 in the negative $\dot{x}$ direction when propagated forward and the stable manifold of L_1 in the positive $\dot{x}$ direction when propagated backwards , as shown in Fig. 14(c)). At a Jacobi constant of $C = 3.10$, the resulting map clearly displays a substantial overlap between these manifold tubes, highlighting a significant region facilitating transit from the exterior to interior via the L_2 and L_1 gateways.

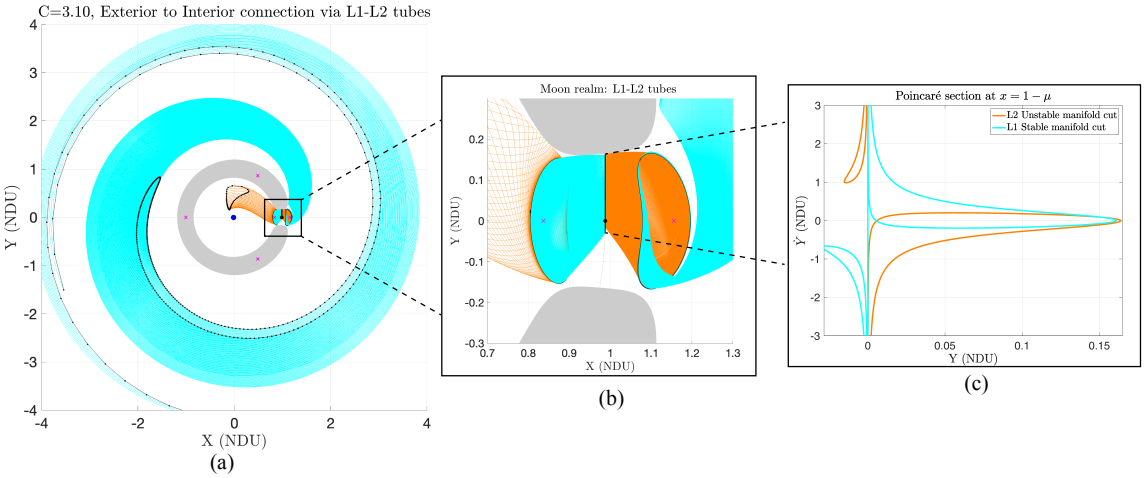

Figure 14: Tube dynamics at $C = 3.10$ with L_1 and L_2 Lyapunov orbit stable and unstable manifolds in exterior, moon and Earth realm. The apogee cut in the exterior and the perigee cut in the Earth realm are depicted using black curves. Insets: (b) showcases intersection of stable L_1 manifold tube and unstable L_2 manifold tube at $x = 1 - \mu$, (c) showcases L_1-L_2 cuts in phase space.

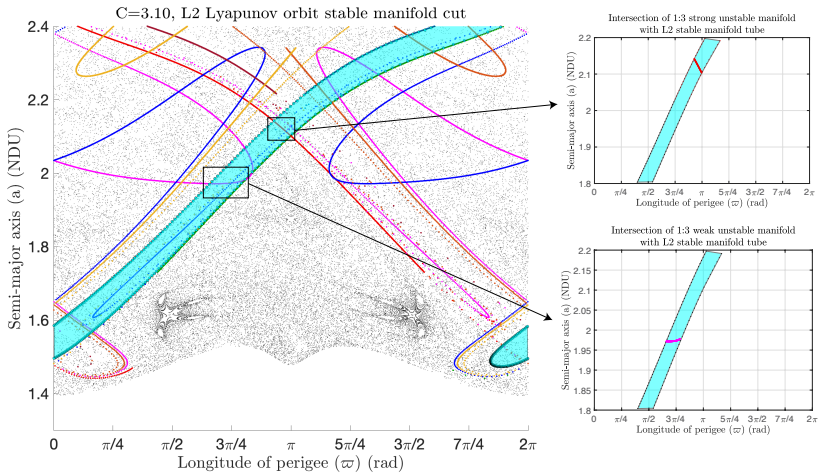

Figure 15: Exterior realm Poincaré section Σ_C at apogee for $C = 3.10$ with L_2 Lyapunov orbit stable manifold cut. Insets showcase intersection of unstable manifold of 1:3 strong and weak unstable resonant orbits with the L_2 Lyapunov stable manifold tube.

Fig. 15 showcases Poincaré map at apogee (Σ_C) for $C = 3.10$, stable and unstable manifolds of 1:3 and 1:4 unstable resonant orbits along with the first cut of the L_2 Lyapunov orbit stable manifold. This cut denotes an "exit" from Σ_C in the exterior realm. All trajectories entering it must emerge in an "entrance" in the Moon realm, as illustrated in Figure 14(a),(b). The tube starts from a resonance region of 1:2 and wraps around the Poincaré map along the semi-major axis. We can clearly see numerous places where the stable manifold tube intersects the unstable manifolds of the 1:3 strong and weak resonant orbit, marking heteroclinic connection between L_2 Lyapunov and 1:3 unstable resonant orbit. Segments of these unstable manifolds residing inside the L_2 stable manifold cut mark transit trajectories. The segment corresponding to minimum stretching is chosen to explore heteroclinic connections (see insets of Fig. 15).

Similarly, Fig. 16 showcases a Poincaré map at perigee in the interior region for $C = 3.10$, stable and unstable manifolds of 2:1 and 3:1 unstable resonant orbits along with the first cut of the L_1 Lyapunov orbit unstable manifold. The region inside the cut would mark the "exit" at the Earth realm for the trajectories

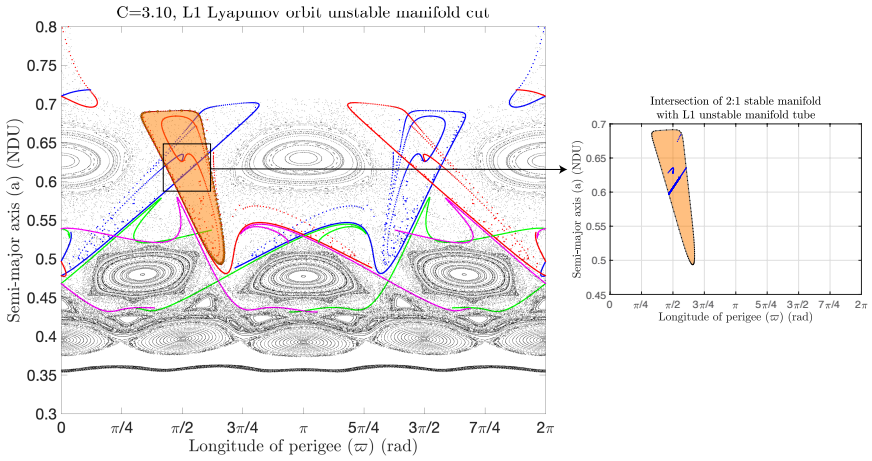

Figure 16: Interior/Earth realm Poincaré section Σ_C at perigee for $C = 3.10$ with L_1 Lyapunov orbit unstable manifold cut. Insets showcases intersection of unstable manifold of 2:1 stable resonant orbit with the L_1 Lyapunov orbit unstable manifold tube.

coming from the Moon or exterior realm. The segment of stable manifold of 2:1 resonant orbit inside the cut and corresponding to minimum stretching is chosen to explore heteroclinic connections between 1:3 and 2:1 unstable resonant orbits (see insets of Fig. 16).

To determine if a heteroclinic connection exists between the interior and exterior regions, it is necessary to confirm intersections between the chosen unstable manifold segment of 1:3 unstable exterior resonant orbit and the chosen stable manifold segment of 2:1 unstable interior resonant orbit within the overlapping region of the L_1 and L_2 tubes on the $x = 1 - \mu$ surface of section. Subsequently, the exterior unstable manifold segment is propagated forward, and the interior stable manifold segment is propagated backward in time until they pierce the $x = 1 - \mu$ section. Fig. 17 shows that initially compact manifold segments evolve into extended curves due to further stretching. A clear intersection between exterior unstable and interior stable manifold segments can be seen inside the overlap region of L_1 and L_2 tubes.

The unstable manifold, significantly stretched, lacks sufficient points to fully capture its shape, resulting in an abrupt transition from the overlapped region onto the L_2 boundary passing through the interior stable manifold. This indicates another heteroclinic connection, albeit less clearly defined and requires interpolation techniques. The trajectory corresponding to the clearly defined heteroclinic connection between the 1:3 strong and 2:1 resonant orbit is illustrated in Fig. 17 (right). We identify that this is a strong unstable exterior resonant orbit as its perigee faces towards the moon.

Precisely determining intersection points demands a high degree of numerical precision. Consequently, points on the unstable manifold (1:3 unstable resonant orbit) and stable manifold (2:1 unstable resonant orbit) nearest to each other are selected to represent the transfer trajectory. The point on the unstable manifold is integrated backward in time, while the point on the stable manifold is integrated forward until both trajectories reach close enough to their respective unstable orbits. The total transfer time is computed to be ≈ 9.5 days. Theoretically, exact convergence to these fixed points would require infinite propagation time due to asymptotic behavior. Operationally, a trajectory is deemed a viable transfer when it approaches sufficiently close to the periodic orbit.

A similar result is see in Fig.18, for the exterior 1:3 weak and interior 2:1 resonant orbit. For the first cut, we again have atleast two heteroclinic connections – one prominently seen and the other hidden due to lack of points and more stretching. The trajectory for the prominent heteroclinic connection between 1:3 weak and 2:1 resonant orbits is shown on the right for which the transfer time is computed to be ≈ 7 days. We identify that this is a weak exterior resonant orbit as it has its perigee facing away from the moon.

Exterior to interior heteroclinic connections are explored between 1:3 strong and weak unstable and 2:1 unstable resonant orbit for $C = 3.15$ in a similar manner, as seen in Fig. 19. For $C = 3.15$ the L_2 Lyapunov orbit tube starts only from the middle of the 1:3 resonance zone and similarly wraps around the phase space. For higher Jacobi constants the starting point of the tube will keep on rising in semi-major axis and it will no longer intersect some of the visible resonant orbit manifolds.

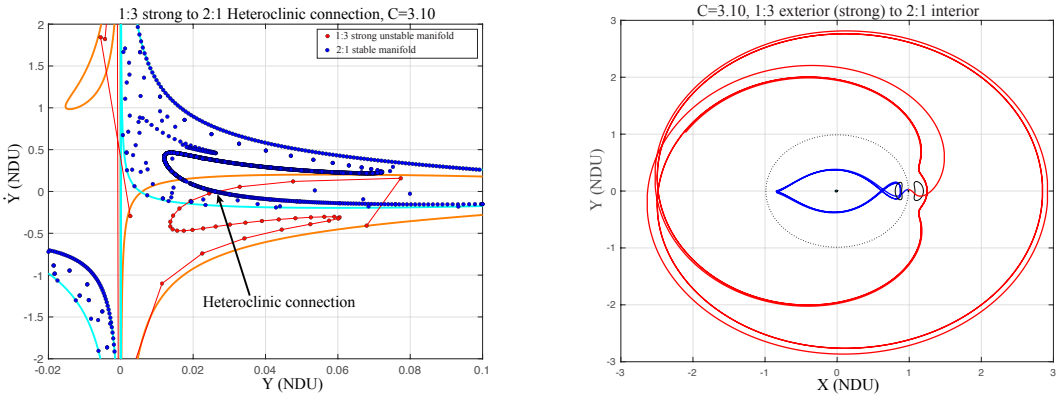

Figure 17: (Left) A heteroclinic connection is found at the overlap of L_1-L_2 tubes. (Right) Transfer trajectory from 1:3 strong unstable resonant orbit to 2:1 unstable resonant orbit.

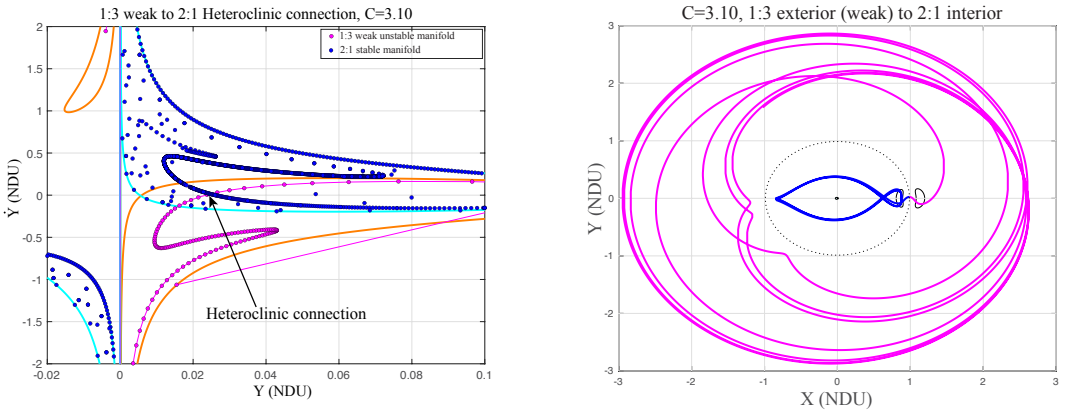

Figure 18: (Left) A heteroclinic connection is found at the overlap of L_1-L_2 tubes. (Right) Transfer trajectory from 1:3 weak unstable resonant orbit to 2:1 unstable resonant orbit.

The overlap region of the L_1 and L_2 stable and unstable manifold cut at $x = 1 - \mu$ drastically diminishes, signifying a notably reduced likelihood of transport between the exterior and interior domains (see subsections of Fig. 19). Overlaying the stable and unstable manifold segments of 2:1 and 1:3 unstable resonant orbits at $x = 1 - \mu$ reveals no heteroclinic connection as they just graze through each other. Attempts were made to identify intersections for the second cut of tubes, but they do not intersect, revealing no overlap region. This establishes that if there were transport from exterior to interior realms at $C = 3.15$, it should have occurred in the first cut only.

Transfers were also explored from 1:3 to 3:1 unstable resonant orbits, which showed similar behavior with two heteroclinic connection points at $C = 3.10$ for both 1:3 strong and weak unstable resonant orbits, and no heteroclinic connection for either at $C = 3.15$.

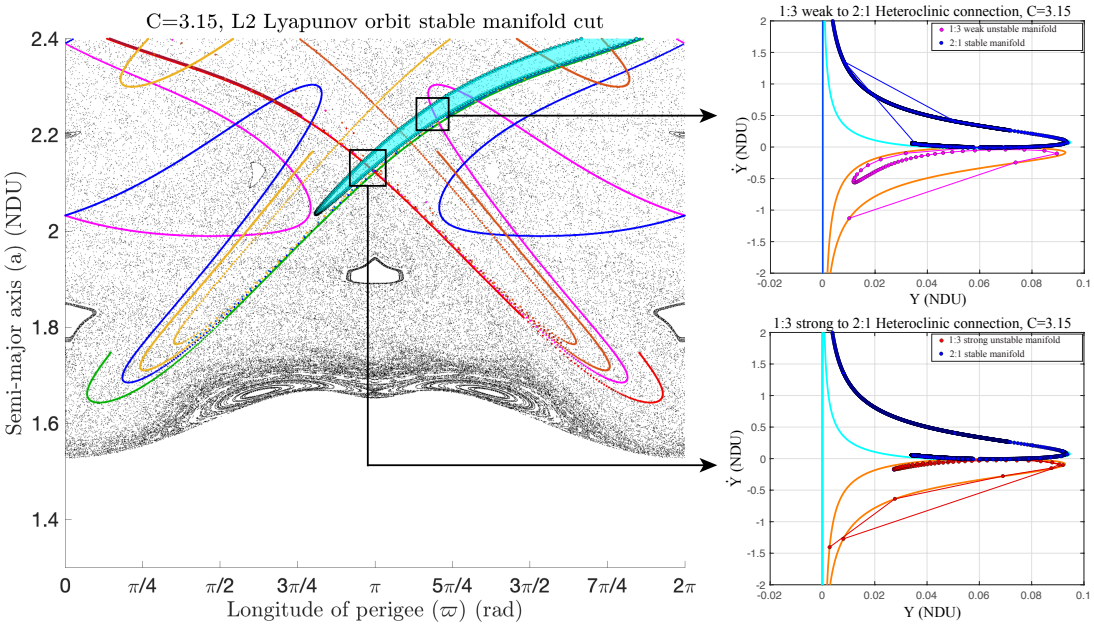

Figure 19: Exterior realm Poincaré section Σ_C at apogee for $C = 3.15$ with L_2 Lyapunov orbit stable manifold cut. Subsections showcases intersection of enclosed segments of unstable manifold of 1:3 strong and weak unstable resonant orbits on $x = 1 - \mu$ section. The L_1-L_2 window is very small and no heteroclinic connection is found.

DISCUSSION AND FUTURE WORK

Poincaré sections at apogee provide a detailed depiction of the rich and complex dynamical structure of the realm exterior to the Moon predominantly occupied by MMRs, highlighting both stable islands and chaotic regions, all depicted in easy-to-visualize geocentric orbital elements. Our results highlight the pronounced impact of exterior resonances of the form $1 : n$, particularly 1:3 and 1:4 resonances, with a special focus on the expansive unstable resonance zones defined by the complex web of its stable and unstable manifolds.

Analysis of unstable resonant periodic orbits has identified the chaotic regions generated by quasi-separatrices of weak unstable resonant orbits embedded within separatrices of strong unstable resonant orbit, which intersect for lower Jacobi constants. Specifically, we have quantified the extent of resonance zones associated with the 1:3 and 1:4 exterior MMRs across three strong unstable orbit families, and depicted them in useful (ϖ, a) and (a, e) planes. Employing these newly established resonance zones for a wider range of MMRs facilitates the formation of an atlas of MMRs, enabling enhanced determination of whether space assets reside in stable or unstable orbital regimes.

Additionally, our study demonstrates the potential for heteroclinic connections between 1:3 unstable exterior and 2:1 and 3:1 unstable interior resonant orbits within feasible time scales ($\approx$ 7-9.5 days) for $C = 3.10$, while no such connections exist for $C = 3.15$. This examination of MMRs using a global dynamics approach (using the CR3BP as a model) enhances our understanding of the intricate dynamics of cislunar space, with implications for mission analysis, mission design, cislunar SDA and operations, and Oterma type transfers.

Future research directions will focus on refining methodologies to precisely determine resonance widths and resonance zones, moving beyond qualitative assessments. Additionally, we aim to explore the influence of 3-dimensionality (e.g., inclination), a significant factor contributing to the presence of secular resonances. Further investigation will involve studying chaotic transport across resonances through analysis of lobe dynamics and flux across chaotic regions. Moreover, we intend to map all prominent resonances in the interior and exterior region to have a global dynamical map of cislunar space up to the Earth's Hill sphere.

Acknowledgments

B.K. was supported in part by the National Science Foundation under Award No. DMS-2202994. This research was also supported by funding from the AFOSR under Award No. FA9550-24-1-0194.

REFERENCES

[1] W. S. Koon, M. W. Lo., J. E. Marsden, and S. D. Ross, "Resonance and capture of Jupiter comets," *Celest. Mech. Dyn. Astron.*, Vol. 81, 2001, pp. 27–38.
[2] O. C. Winter and C. D. Murray, "Resonance and chaos. II. Exterior resonances and asymmetric libration," *Astron. Astrophys.*, Vol. 328, 1997, pp. 399–408.
[3] R. Malhotra and Z. Chen, "Non-perturbative investigation of low-eccentricity exterior mean motion resonances," *Mon. Not. R. Astron. Soc.*, Vol. 521, 2023, pp. 1253–1263.
[4] X. Li, Y.-J. Qian, X.-D. Yang, and W. Zhang, "Stability and bifurcation analyses for exterior resonant families in Earth-Moon system," *Results Phys.*, Vol. 31, 2021, p. 104961 (12 pp.).
[5] L. Lan and R. Malhotra, "Neptune's resonances in the scattered disk," *Celest. Mech. Dyn. Astron.*, Vol. 131, 2019, p. 39 (26 pp.).
[6] B. Kumar and R. L. Anderson, "A survey of Oberon mean motion resonant unstable orbit properties and connections for Uranian tours," *AAS/AIAA Astrodynamics Specialist Conference*, Broomfield, CO, Paper AAS 24-288, 2024.
[7] A. Rawat, B. Kumar, A. J. Rosengren, and S. D. Ross, "Resonance widths, chaotic zones, and transport in cislunar space," *AAS/AIAA Astrodynamics Specialist Conference*, Broomfield, CO, Paper AAS24-368, 2024.
[8] W. S. Koon, M. W. Lo, J. E. Marsden, and S. D. Ross, *Dynamical Systems, the Three-Body Problem and Space Mission Design*. Marsden Books, 2022.
[9] J. D. Meiss and E. Ott, "Markov tree model of transport in area-preserving maps," *Phys. D.*, Vol. 20, 1986, pp. 387–402.
[10] C. G. Schroer and E. Ott, "Targeting in Hamiltonian systems that have mixed regular/chaotic phase spaces," *Chaos*, Vol. 7, 1997, pp. 512–519.
[11] S. Wiggins, "On the geometry of transport in phase space I. Transport in k-degree-of-freedom Hamiltonian systems, $2 \leq k \leq \infty$," *Phys. D.*, Vol. 44, 1990, pp. 471–501.
[12] J. D. Meiss, "Symplectic maps, variational principles, and transport," *Rev. Mod. Phys.*, Vol. 64, 1992, pp. 795–848.

[13] S. D. Ross and D. J. Scheeres, "Multiple gravity assists, capture, and escape in the restricted three-body problem," *SIAM J. Appl. Dyn. Syst.*, Vol. 6, 2007, pp. 576–596.
[14] M. A. Werner, "Multiple Gravity Assists for Low Energy Transport in the Planar Circular Restricted 3-Body Problem," Master's thesis, Virginia Tech, 2022.
[15] J. S. Parker and R. L. Anderson, *Low-Energy Lunar Trajectory Design*. Hoboken: Wiley, 2014.
[16] B. Kumar, R. L. Anderson, and R. de la Llave, "High-order resonant orbit manifold expansions for mission design in the planar circular restricted 3-body problem," *Commun. Nonlinear Sci. Numer. Simul.*, Vol. 97,, 2021, p. 105691 (15 pp.).
[17] À. Haro, M. Canadell, J. Figueras, *et al.*, *The Parameterization Method for Invariant Manifolds*. Cham: Springer, 2016.
[18] B. Kumar, R. L. Anderson, and R. de la Llave, "Rapid and accurate methods for computing whiskered tori and their manifolds in periodically perturbed planar circular restricted 3-body problems," *Celest. Mech. Dyn. Astron.*, Vol. 134,, 2021, p. 3 (38 pp.).
[19] K. C. Howell, D. C. Davis, and A. F. Haapala, "Application of periapse maps for the design of trajectories near the smaller primary in multi-body regimes," *Math. Probl. Eng.*, Vol. 2012, 2012, p. 351759 (22 pp.).
[20] S. Balasuriya, "Dynamical systems techniques for enhancing microfluidic mixing," *Journal of Micromechanics and Microengineering*, Vol. 25, 08 2015, p. 094005.
[21] B. Kumar and A. Moreno, "Networks of periodic orbits in the Earth–Moon system through a regularized and symplectic lens," *AAS/AIAA Astrodynamics Specialist Conference*, Boston, MA, Paper AAS 25-677, 2025.
[22] R. Rimmer, "Symmetry and bifurcation of fixed points of area preserving maps," *J. Differ. Equ.*, Vol. 29, 1978, pp. 329–344.
[23] V. Rom-Kedar and S. Wiggins, "Transport in two-dimensional maps," *Arch. Ration. Mech. Anal.*, Vol. 109, 1990, pp. 239–298.
[24] W. S. Koon, J. E. Marsden, S. D. Ross, , M. W. Lo., and D. J. Scheeres, "Geometric mechanics and the dynamics of asteroid pairs," *Ann. N. Y. Acad. Sci.*, Vol. 1017, 2004, pp. 11–38.
[25] M. Dellnitz, O. Junge, W. S. Koon, *et al.*, "Transport in dynamical astronomy and multibody problems," *Int. J. Bifurc. Chaos*, Vol. 15, 2005, pp. 699–727.
[26] S. D. Ross and P. Tallapragada, "Detecting and exploiting chaotic transport in mechanical systems," *Applications of Chaos and Nonlinear Dynamics in Science and Engineering* (S. Banerjee, L. Rondoni, and M. Mitra, eds.), pp. 155–183, New York: Springer, 2012.
[27] S. Naik, F. Lekien, and S. D. Ross, "Computational method for phase space transport with applications to lobe dynamics and rate of escape," *Regul. Chaotic Dyn.*, Vol. 22, 2017, pp. 272–297.
[28] J. M. Greene, R. S. MacKay, F. Vivaldi, and M. J. Feigenbaum, "Universal behaviour in families of area-preserving maps," *Phys. D.*, Vol. 3, 1981, pp. 468–486.
[29] W. S. Koon, M. W. Lo., J. E. Marsden, and S. D. Ross, "Heteroclinic connections between periodic orbits and resonance transitions in celestial mechanics," *Chaos*, Vol. 10, 2000, pp. 427–469.
[30] S. D. Ross, "Trade-off between fuel and time optimization," *New Trends in Astrodynamics and Applications*, College Park, MD, 2003.
[31] N. Hiraiwa, M. Bando, I. Nisoli, and Y. Sato, "Designing robust trajectories by lobe dynamics in low-dimensional Hamiltonian systems," *Phys. Rev. Research*, Vol. 6, 2024, p. L022046 (5 pp.).